Crystal structure regulation of $CoSe_2$ induced by Fe dopant for promoted surface reconstitution toward energetic oxygen evolution reaction

Shuo Chen[1,2], Kaiqin Yue[2], Jiawei Shi[1], Zhicheng Zheng[2], Yuanqing He[2], Hao Wan[1,], Gen Chen[2], Ning Zhang[2], Xiaohe Liu[1,2]*, Renzhi Ma[3,]**

[1] Zhongyuan Critical Metals Laboratory & School of Chemical Engineering, Zhengzhou University, Zhengzhou 450001, P. R. China.

[2] School of Materials Science and Engineering, Central South University, Changsha, Hunan 410083, P. R. China.

[3] International Center for Materials Nanoarchitectonics (WPI-MANA), National Institute for Materials Science (NIMS), Namiki 1-1, Tsukuba, Ibaraki 305-0044, Japan.

* Correspondence: wanhao@zzu.edu.cn (H. Wan); liuxh@csu.edu.cn (X. Liu); MA.Renzhi@nims.go.jp (R. Ma)

KEYWORDS: doping, transition metal selenide, phase transition, surface reconstitution, electrocatalytic oxygen evolution reaction

Abstract

Most non-oxide catalysts based on transition metal elements will inevitably change their primitive phases under anodic oxidation conditions in alkaline media. Establishing a relationship between bulk phase and surface evolution is imperative to reveal the intrinsic catalytic active sites. In this work, it is demonstrated that the introduction of Fe facilitates the phase transition of orthorhombic $CoSe_2$ into its cubic counterpart, and then accelerates the Co-Fe hydroxide layer generation on the surface during electrocatalytic oxygen evolution reaction (OER). As a result, the Fe-doped cubic $CoSe_2$ catalyst exhibits exhibited a significantly enhanced activity with a considerable overpotential decrease of 79.9 and 66.9 mV to deliver 10 mA cm^{-2} accompanied by a Tafel slope of 48.0 mV dec^{-1} toward OER when compared to orthorhombic $CoSe_2$ and Fe-doped orthorhombic $CoSe_2$, respectively. Density Function Theory (DFT) calculation reveals that the introduction of Fe on the surface hydroxide layers will tune electron density around Co atoms and raise the d-band center. These findings will provide deep insights into the surface reconstitution of OER electrocatalysts based on transition metals.

KEYWORDS: doping, transition metal selenide, phase transition, surface reconstitution, electrocatalytic oxygen evolution reaction

Introduction

Electrochemical water splitting, a green approach for hydrogen (H_2) generation, is greatly cherished as a far-reaching design for energy structure transition and thus achieves carbon neutralization[1, 2, 3]. The anodic half-reaction of oxygen evolution reaction (OER) involving a four-electron-transfer process is considered as the bottleneck for efficient overall water splitting due to its sluggish kinetics[4]. At present, high-performance OER catalysts are mainly noble metal-based catalysts (e.g. IrO_2 and RuO_2) with unique electronic structures and ideal sorption/desorption properties on intermediates, however, suffering from severe scarcity and high cost[5, 6]. Therefore, it has become a research hotspot to develop non-precious catalysts with high activity and durability toward OER.

Numerous efforts have been devoted to designing non-precious catalysts including transition metal oxides[7], hydroxides[8, 9, 10], chalcogenides[11] and phosphides[12, 13], *etc*. For most non-oxide catalysts based on metal elements, an *in situ* evolution occurs on the surface of the bulk phase during the OER process, and a hydroxylation layer thus forms, which is considered as the actual active species for oxygen evolution[14, 15, 16]. For instance, it has been proposed that due to facile surface reorganization, transition metal selenides show an ideal oxidation layer with a certain thickness and significant OER catalytic activity[17]. In alkaline media, Se atoms will dissolve out, and the *in-situ* generated nickel hydroxide is responsible for their activity[18]. Therefore, rigorous investigations on the surface reactive phases are imperative to figure out the actual catalytic enhancement mechanism with a particular focus on the relationship between the surface structure and the electrocatalytic process [19, 20].

Cobalt selenide ($CoSe_2$) has emerged with great potency as a bifunctional electrocatalyst for OER and hydrogen evolution reaction (HER) because of its unique catalytic performance[21, 22]. To further improve the electrocatalytic activity, nonmetallic atom substitution has been extensively adopted to optimize the interior coordination environment. Moreover, the lattice

distortion induced by heteroatoms could influence the local symmetry and might even cause structural phase transformation. It has been demonstrated that phosphorus (P) dopant could induce the phase transition of $CoSe_2$ from cubic to orthorhombic phases and thus enhance the HER activity[23]. Besides, dopants can also affect the structural stability in alkaline media during the electrocatalytic process[19, 21]. However, investigations on how metallic dopants influence the surface structure of $CoSe_2$ during the OER process have been rarely unveiled. Since the phase transition during the OER in alkaline electrolytes for $CoSe_2$ is universal, it inspires us to re-consider whether heterogeneous metallic dopants can regulate the surface oxidation during alkaline OER as well as whether the "extremely robust stability" is helpful to OER.

Herein, cubic and orthorhombic Fe-doped $CoSe_2$ (denoted as *c*-$Co_{2/3}Fe_{1/3}Se_2$ and *o*-$Co_{2/3}Fe_{1/3}Se_2$, respectively), and orthorhombic $CoSe_2$ (named as *o*-$CoSe_2$) nanostructures were successfully prepared through metal doping and the subsequent selenium annealing. Among them, *c*-$Co_{2/3}Fe_{1/3}Se_2$ exhibited the best intrinsic OER activity, *i.e.* an overpotential of 254.7 mV delivering a current density of 10 mA cm^{-2} accompanied with a Tafel slope of 48.0 mV dec^{-1}. Based on the *ex-situ* characterizations on the phase structure of catalysts before and after the OER process, it has been unveiled how Fe dopants influence the surface structure of $CoSe_2$ during the OER process. A migration hypothesis was thus proposed for *c*-$Co_{2/3}Fe_{1/3}Se_2$ catalyst that Fe atoms were not stable in the selenide lattice, which would migrate into alkaline electrolytes easily and participate in the Co oxidation on the surface. DFT calculations illustrate the role of Fe atoms in the newly formed hydroxide layer. These findings will provide new perspectives on the relationship among surface evolution, bulk phase structure, and OER activity.

Experiment section

Chemicals

Cobalt (II) chloride hexahydrate ($CoCl_2 \cdot 6H_2O$, Sinopharm Group China, >98%), iron(II) chloride tetrahydrate ($FeCl_2 \cdot 4H_2O$, Fujifilm Wako Pure Chemical Corporation, >99%), hexamethylenetetramine (HMT, Sinopharm Group China), sodium anthraquinone−2-sulfonate (AQS, Aladdin Reagent Group, >97%), selenium powder (Se Sinopharm Group China, >99%), potassium hydroxide (KOH, Sinopharm Group China, >85%), ethanol (C_2H_5OH, Sinopharm Group China, ≥99.9%) and Nafion dispersion (5 wt %, Alfa Aesar) were used directly without any further purification. Carbon paper (Toray) was cleaned with ethanol and deionized water successively.

Synthesis of Co_2Fe_1-LDH (layer double hydroxide) and Co-LDH precursors

Layer double hydroxide was synthesized by a simple coprecipitation process assisted by an oil bath according to our previous work[24]. Typically, 5 mmol $CoCl_2 \cdot 6H_2O$, 2.5 mmol $FeCl_2 \cdot 4H_2O$, 5 mmol AQS, and 10 mmol HMT were dissolved in 500 mL deionized water. The homogeneous solution was refluxed under 120 ℃ for 6 hours. Cooling to room temperature, the yellow precipitate was collected by centrifugation and then washed with ethanol and deionized water several times. The precursor was dried at 60 °C overnight in a vacuum, and then Co_2Fe_1-LDH precursor was obtained. The Co/Fe molar ratio of CoFe-LDH was tuned by adjusting the feed ratio, while Co-LDH was synthesized with the absence of $FeCl_2 \cdot 4H_2O$ while keeping other conditions the same.

Synthesis of o-$CoSe_2$ and c-$Co_{2/3}Fe_{1/3}Se_2$

Selenides were prepared through a high-temperature annealing process[25]. In brief, the LDH precursor and Se powder with a mass ratio of 1:3 were mixed adequately by grinding in a mortar. The mixture was placed in a porcelain crucible and heated at 450℃ with a heating rate of 2 ℃

min $^{-1}$ in a 5% H_2/Ar atmosphere. Black selenides were attained after cooling to ambient temperature. Using Co_2Fe_1-LDH and Co-LDH as the starting materials, *o*-$CoSe_2$ and *c*-$Co_{2/3}Fe_{1/3}Se_2$ were prepared, separately.

Synthesis of o-$Co_{2/3}Fe_{1/3}Se_2$

The *o*-$Co_{2/3}Fe_{1/3}Se_2$ was prepared by replacing the 5% H_2/Ar atmosphere with pure Ar with other high-temperature annealing conditions the same as those for *c*-$Co_{2/3}Fe_{1/3}Se_2$.

Material characterizations

X-ray powder diffraction (XRD) patterns were recorded at a Rigaku D/max 2500 powder X-ray diffractometer with Cu Kα radiation. Scanning electron microscopy (SEM) and energy dispersive X-ray spectroscopy (EDS) data were collected on a Tescan Mira 3 field emission scanning electron microscope operated at 5 kV with an EDS detector. Transmission electron microscopy (TEM), selected area electron diffraction patterns (SAED), high-resolution transmission electron microscopy (HRTEM), and high-angle annular dark-field imaging (HAADF) images were obtained from a Talos F200X field-emission high-resolution transmission electron microscope. X-ray photoelectron spectroscopy (XPS) data were recorded on a Thermo Scientific K-Alpha with Al Kα radiation (hν = 1486.6 eV) and the binding energy scale was calibrated by referencing C 1s signal as 284.80 eV. Raman spectra were obtained by a HORIBA Scientific LabRAM HR Evolution. Inductively coupled plasma (ICP) spectroscopy was carried out on a PB avio 200.

Electrochemical measurements

Electrochemical tests were carried out on a CHI 760E electrochemical workstation coupled with a standard three-electrode system. For the preparation of the working electrode, 4 mg catalyst was dispersed in the mixture of 490 μL alcohol, 490 μL deionized water, and 20 μL Nafion solution (5 wt%) to form a homogeneous ink. 100 μL of the as-prepared ink was dripped

on a piece of carbon paper (1 cm × 1cm with one side covered completely by Teflon tape) and then dried at 105 °C. The catalyst loading was unified as 0.4 mg cm^{-2}. A Hg/HgO electrode (containing an interior electrolyte of 1.0 M KOH) and graphite rod were used as reference electrode and counter electrode, respectively. All the measured potentials (denoted as $E_{Hg/HgO}$) were converted to the reversible hydrogen electrode (RHE) form according to the following equation in which 0.098V stood for the potential value of Hg/HgO versus the normal hydrogen electrode:

$$E_{RHE}=E_{Hg/HgO}+0.098\ V+pH\times 0.059$$

Before each electrochemical test, the working electrode was activated by cycling the potential from 0 to 1.20 V versus Hg/HgO fifty times at a scan rate of 30 mV s^{-1}. Linear sweep voltammetry (LSV) was conducted by scanning the samples in the potential scope of 0 - 1.20 V versus Hg/HgO at a scan rate of 5 mV s^{-1} with 95% iR compensation. Double-layer capacitance (C_{dl}) linearly proportional to ECSA was measured by cyclic voltammetry (CV) curves within the non-Faradaic potential window between 0.2 and 0.3 V versus Hg/HgO at various scan rates (20, 40, 60, 80 and 100 mV s^{-1}). From the plots of the difference between the anodic and cathodic current densities at 0.25V versus Hg/HgO against the scan rates, the C_{dl} value of a catalyst was determined as half of the slope. Electrochemically active surface area (ECSA) was then calculated following the following equation:

$$ECSA = C_{dl} / 0.04\ mF\ cm^{-2}$$

EIS was collected in the frequency range from 10000 to 0.1 Hz with an external voltage of 0.60 V versus Hg/HgO. A chronopotentiometry measurement was carried out at a constant current density of 20 mA cm^{-2}.

DFT calculations

Density functional theory (DFT) calculations within CASTEP packages were applied in this work to reveal the electronic structure. The generalized gradient approximation (GGA) and Perdew–Burke–Ernzerhof (PBE) were chosen for all the calculations. Accordingly, the plane-wave basis cutoff energy was set to 380 eV with the fine quality selection and the ultrasoft pseudopotentials. In addition, we also applied the Limited Broyden–Fletcher–Goldfarb–Shannon (LBFGS) algorithm in this work with the costumed k-point set of 2*2*1 to balance the calculation accuracy and efficiency. For all models, 15 Å vacuum space in the z-axis was fixed to supply sufficient space for geometry relaxations. For the geometry optimization, the following convergence criteria were applied, which are the Hellmann-Feynman forces should be less than 0.03 eV $Å^{-1}$, the total energy difference should not exceed 5×10^{-5} eV per atom, and the inter-ionic displacement should be smaller than 0.001 $Å^{-1}$.

Results and discussion

As illustrated in **Figure 1**a, *o*-$CoSe_2$ and *c*-$Co_{2/3}Fe_{1/3}Se_2$ were prepared through a selenylation annealing process under a 5% H_2/Ar atmosphere using Co-LDH and Co_2Fe_1-LDH obtained from the coprecipitation procedure as the precursor, respectively. X-ray diffraction (XRD) was used to detect the crystalline phase compositions. As shown in Figure 1b, Co-LDH sample was indexed as a typical LDH phase. After the introduction of Fe^{3+} ions, the (012) diffraction of the precursor (the pink trace) exhibits a positive shift, suggesting a lattice contraction but also confirming the doping behavior. After the selenylation treatment in 5% H_2/Ar flow, Co-LDH was converted into orthorhombic $CoSe_2$ (JCPDS#53-0449, space group *Pnnm*), as evidenced by the purple XRD pattern in Figure 1c. **Figure S1** displays the XRD pattern of the product treated under unitary Ar atmosphere, by which orthorhombic selenide structure was also indexed. When replacing Co-LDH with the Co_2Fe_1-LDH as the precursor, the cubic selenide phase (JCPDS #09-0234, space group Pa-3) is detected, which is similar to some previous works. This result suggests the phase transition after the introduction of Fe atoms, as depicted in Figure 1d. While *o*-$Co_{2/3}Fe_{1/3}Se_2$ was prepared by annealing under pure Ar atmosphere. It should be noted that both the (011) and (101) peaks of *o*-$Co_{2/3}Fe_{1/3}Se_2$ exhibit a positive shift by ~0.22° compared with those of *o*-$CoSe_2$, indicating a small lattice contraction that might be caused by the substitution of Fe atoms. Based on the above results, it is concluded that the introduction of Fe dopant can lead to the lattice contraction of LDH precursor but also promote phase transformation during the selenylation treatment when 5% H_2/Ar flow was adopted.

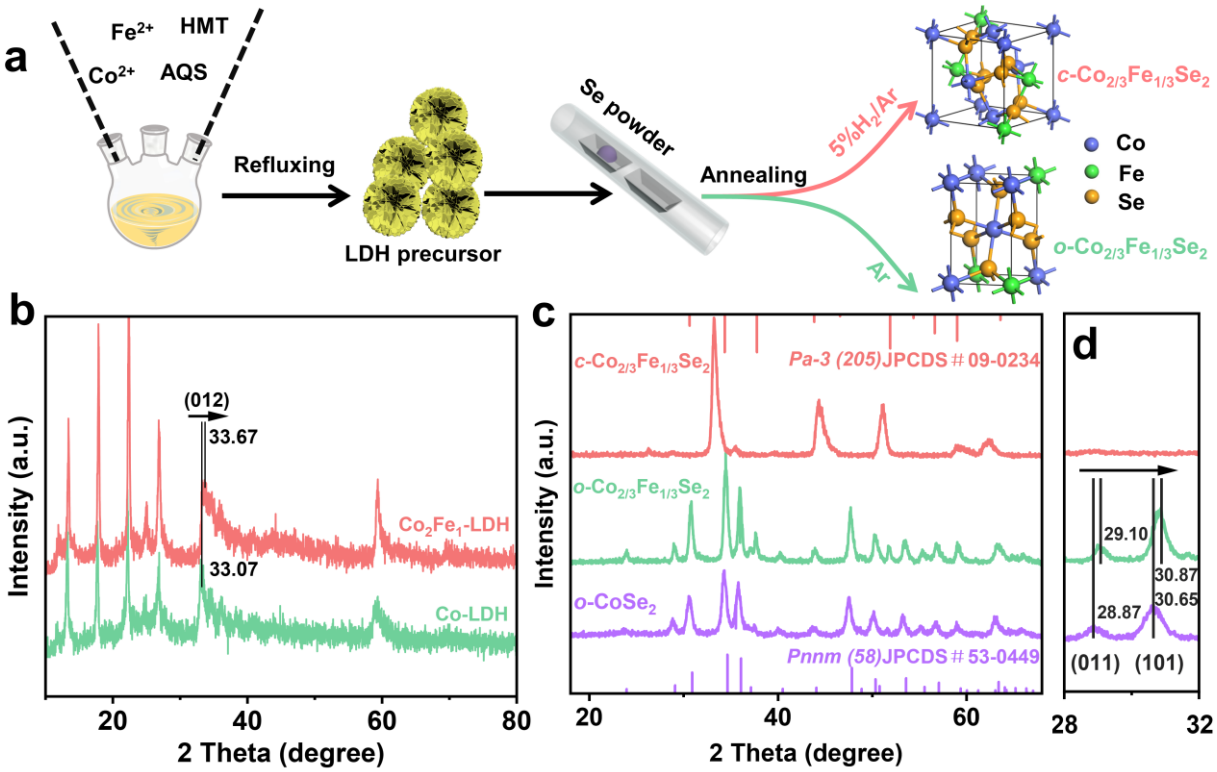

Figure 1. Material synthesis and phase structure characterizations. (a) Schematic illustration for the preparation of *c*-$Co_{2/3}Fe_{1/3}Se_2$ and *o*-$Co_{2/3}Fe_{1/3}Se_2$. XRD patterns of (b) LDH precursors and (c) selenide phases. (d) The magnification of (c) in the scope of 28 - 32°.

The micro-/nano-structural details of the as-prepared samples were investigated using SEM and TEM. **Figure S2** shows the morphological and compositional information of the LDH precursors, from which it can be seen that Co_2Fe_1-LDH is of hierarchical nanoflowers assembled by nanosheets. The compositional analysis further confirmed the successful introduction of Fe content into Co_2Fe_1-LDH precursor. After the high-temperature selenylation process, the hierarchical nanostructure was severely damaged, as depicted in **Figure S3**. EDS data, as shown in **Figure S4**, suggest that the molar ratio of Co: Fe: Se is about 1.7: 1: 4.2 for *c*-$Co_{2/3}Fe_{1/3}Se_2$, which is rather close to that for *o*-$Co_{2/3}Fe_{1/3}Se_2$ (1.8 : 1: 3.6). **Figure 2**a demonstrates *o*-$Co_{2/3}Fe_{1/3}Se2$ lattice with interplanar spacing of 0.265 nm, corresponding to the (111) planes. In Figure 2d, the lattice fringes of 0.310 nm correspond to the (200) lattice planes of *c*-$Co_{2/3}Fe_{1/3}Se_2$. The corresponding SAED patterns in Figure 2b and 2e with bright spots also

confirm the phase transition. Elemental maps, as shown in Figure 2c and 2f, overlap with the profiles of the selenides, revealing that all of the Co, Fe, and Se elements are homogeneously distributed over *c*-$Co_{2/3}Fe_{1/3}Se_2$ and *o*-$Co_{2/3}Fe_{1/3}Se_2$ nanostructures.

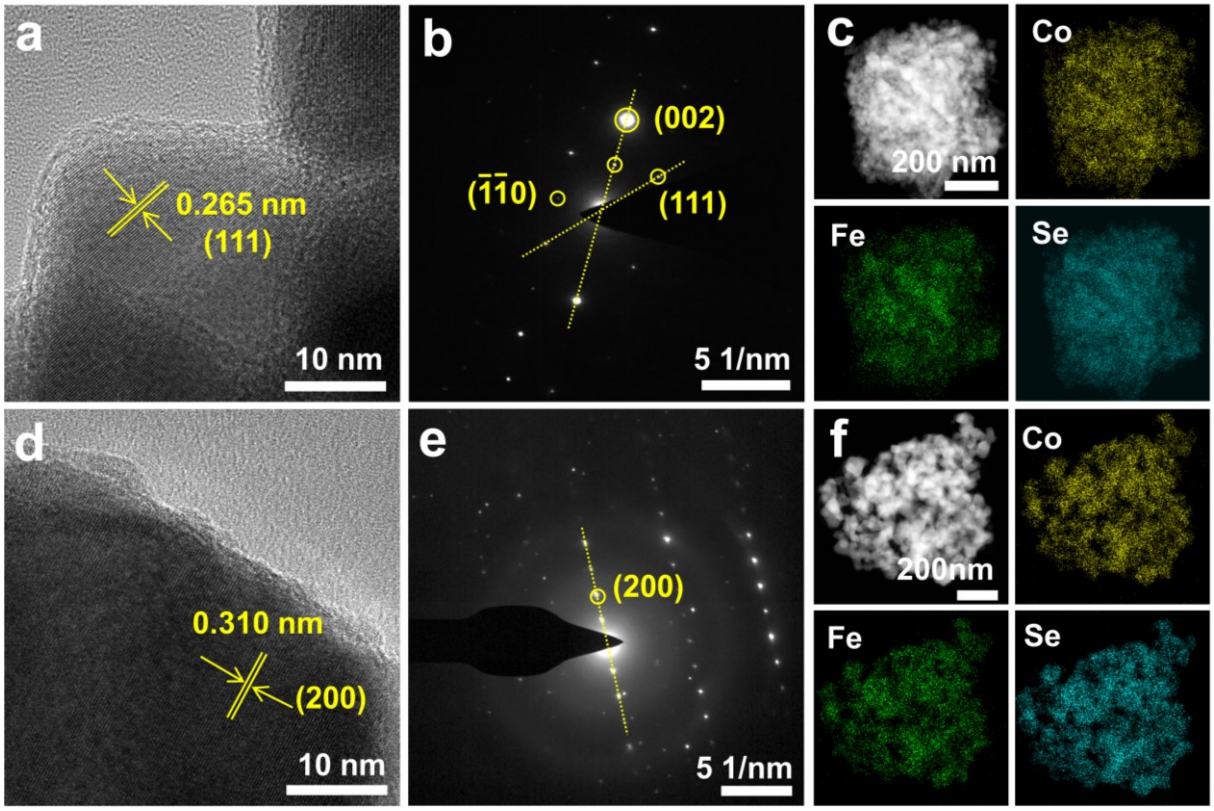

Figure 2. TEM characterizations. (a, d) HRTEM images, (b, e) SAED patterns, and (c, f) elemental mapping of *o*-$Co_{2/3}Fe_{1/3}Se_2$ and *c*-$Co_{2/3}Fe_{1/3}Se_2$, respectively.

Raman and XPS measurements were carried out to verify the surface chemical environment as well as the phase change mechanism. The peaks at ~186.8 nm^{-1} and 261.7 nm^{-1} are attributed to the Se-Se librational models and stretching vibrations, separately (**Figure 3**a)[26]. The librational signal exhibits a red shift when Fe atoms are introduced to the orthorhombic lattice and further reveals an obvious shift to 169.3 nm^{-1} when the bulk phase structure is converted into cubic. It has been unveiled that the shift is closely related to the local symmetry and Fe atoms order can increase the local symmetry of *Pnnm*[27]. As the faint variation spreads to a certain extent, the dominant phase transforms from orthorhombic (*Pnnm*) to cubic (*Pa-3*). Compared to those of *o*-$CoSe_2$, the peaks of *c*-$Co_{2/3}Fe_{1/3}Se_2$ demonstrate a diametrically

opposite shift, indicating the Se-Se bond or the unit cell shows expansion (186.8 nm^{-1}) and compression (261.7 nm^{-1}) along the specific crystal orientations. The overall XPS survey spectra, as depicted in **Figure S5**, certify the co-presence of Co, Fe, and Se in three samples. Fe 2p signal is divided into spin-orbital splitting peaks of Fe-Se bond, Fe-O bond, and extra shake-up satellite peaks (Figure 3b)[28], in which the Fe-Se $2p_{3/2}$ peak of *c*-$Co_{2/3}Fe_{1/3}Se_2$ exhibited a negative shift of 0.2 eV compared with that of *o*-$Co_{2/3}Fe_{1/3}Se_2$. In addition, the ratio of Fe-Se: Fe-O in *c*-$Co_{2/3}Fe_{1/3}Se_2$ decreased based on the area ratio of the corresponding fitting peaks (**Table S1**), both of which indicate Fe atoms in the cubic crystal system possess higher electron cloud density. Co 2p spectrum of *o*-$CoSe_2$, as shown in Figure 3c, confirms the co-existence of Co-Se and Co-O bonds (the latter may originate from the inevitable surface oxidation)[21, 29, 30]. In comparison, Co-Se $2p_{3/2}$ of *o*-$Co_{2/3}Fe_{1/3}Se_2$ and *c*-$Co_{2/3}Fe_{1/3}Se_2$ show a positive shift by 0.11 and 0.41 eV respectively, revealing an electron loss of Co ions in *o*-$Co_{2/3}Fe_{1/3}Se_2$ and *c*-$Co_{2/3}Fe_{1/3}Se_2$ with the doping of Fe. The ratio of Co-Se: Co-O in *c*-$Co_{2/3}Fe_{1/3}Se_2$ is the largest among the three samples, indicating that Co atoms lose more electrons in the electron coupling effect. It is widely accepted that the high-valence Co species prefer to convert into reactive oxygen intermediate (i.e. CoOOH) which is significant to strengthen the OER activity[31]. Se 3d spectrum consists of three peaks, i.e. the Se-O bond and two metal-Se spin-orbital peaks (Figure 3d). Se-O bond is mainly attributed to the unavoidable surface oxidation in the air[32]. The Se $3d_{5/3}$ signals of *o*-$CoSe_2$ and *o*-$Co_{2/3}Fe_{1/3}Se_2$ almost overlap, however, show an enormous shift to higher binding energy compared to that of *c*-$Co_{2/3}Fe_{1/3}Se_2$. The results suggest that the electron interaction in the cubic symmetry is much stronger, which may optimize the *d*-band electronic structure and thus tune ideal adsorption properties on reactant and/or intermediates[33].

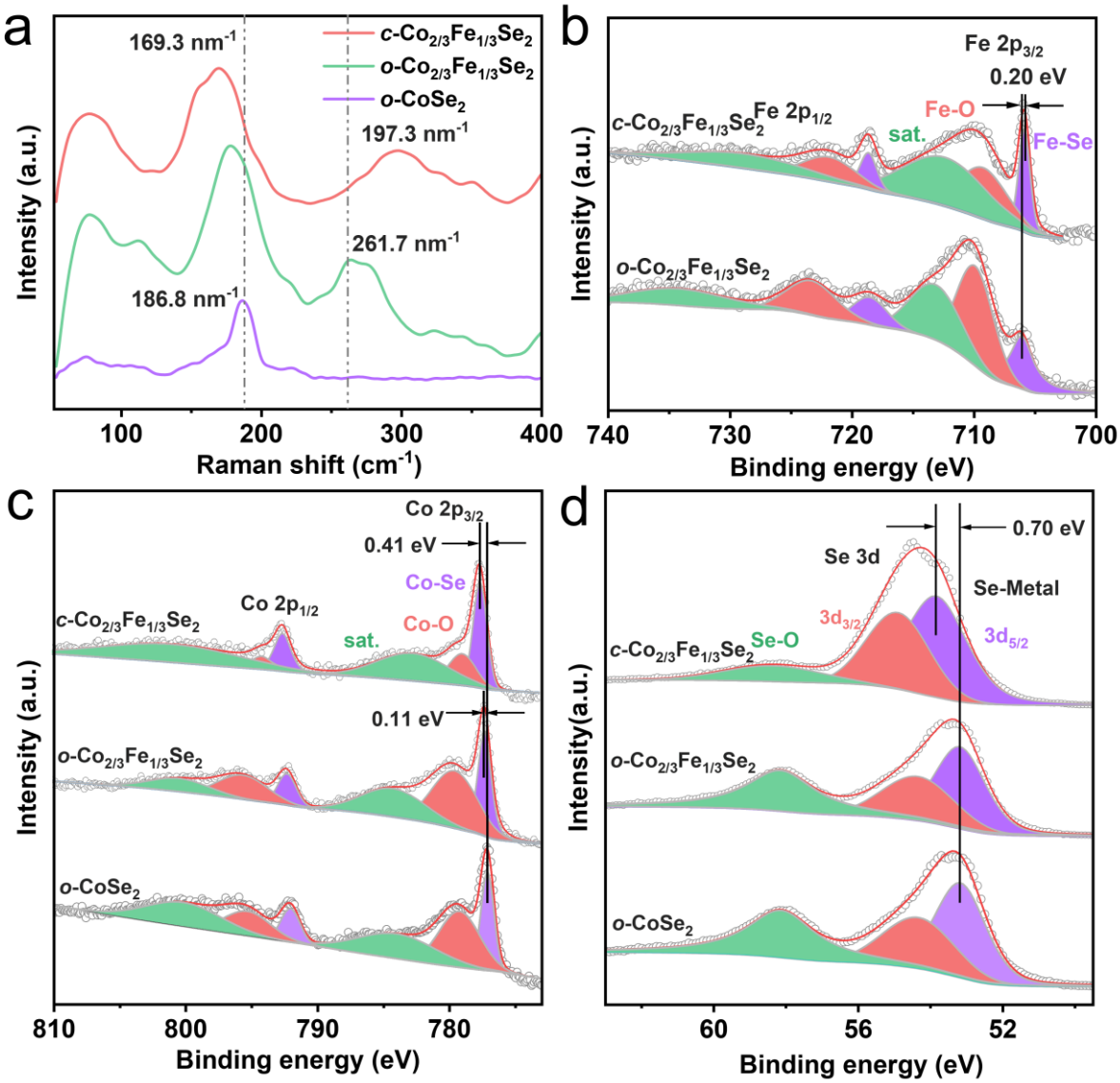

Figure 3. Electronic structure. (a) Raman spectra of *c*-$Co_{2/3}Fe_{1/3}Se_2$, *o*-$Co_{2/3}Fe_{1/3}Se_2$, and *o*-$CoSe_2$. XPS spectra of (b) Fe 2p, (c) Co 2p, and (d) Se 3d of different selenide nanostructures.

To evaluate the influence of crystal structure on OER activity, detailed electrochemical tests were conducted in 1.0 M KOH. LSV curves, as can be seen in **Figure 4**a-b, suggest Fe doping could increase the OER activity of *o*-$CoSe_2$. Moreover, *c*-$Co_{2/3}Fe_{1/3}Se_2$ exhibits a greatly reduced OER overpotential (254.7 mV) by ~67 mV and 80 mV to deliver a current density of 10 mA cm^{-2} compared with *o*-$Co_{2/3}Fe_{1/3}Se2$ (321.6 mV) and *o*-$CeSe_2$ (334.6 mV), separately. It was mentioned that the *c*-$Co_{2/3}Fe_{1/3}Se_2$ exhibits outstanding OER performance compared to some recently reported catalysts (**Table S2**). Tafel slope is also used to investigate the reaction kinetics and the rate-determining step (Figure 4c). *c*-$Co_{2/3}Fe_{1/3}Se_2$ offers the smallest slope of

48.0 mV dec^{-1} while the two orthorhombic catalysts almost keep the same values of ~60 mV dec^{-1}, implying that the cubic cell possesses a faster catalytic kinetic process with the first electron transfer step followed by rate-determining chemical transformation[34]. The Nyquist plots in Figure 4d suggest that c-$Co_{2/3}Fe_{1/3}Se_2$ possesses the minimum charge transfer resistance (3.17 Ω) compared with 15.48 Ω for *o*-$Co_{2/3}Fe_{1/3}Se_2$ and 60.12 Ω for *o*-$CoSe_2$ (**Table S3**), indicating that Fe dopant dramatically accelerated the interfacial kinetics and the phase transition could further enhance this effect. By plotting the current density against CV scan rates in the non-Faradaic potential window, the electrochemical active surface area (ECSA) linearly proportionating to C_{dl} (double-layer capacitance) was evaluated, as presented in Figure 4e. It's worth noting that *o*-$CoSe_2$ exhibits the largest C_{dl} value of 24.63 mF cm^{-2} and Fe dopant substantially decreases the active surface area. In particular, *c*-$Co_{2/3}Fe_{1/3}Se_2$ exposed more active sites compared with *o*-$Co_{2/3}Fe_{1/3}Se_2$. The specific ECSA value was calculated according to the specific capacitance (0.04 mF cm^{-2})[35] for an ideal flat surface (insert in Figure 4f). To further clarify the relationship between surface area and catalytic activity, the ECSA-normalized current density was presented in Figure 4f. The redox peak at around 1.4 V is attributed to the $Co^{2+} \rightarrow Co^{3+}$ oxidation and thus *c*-$Co_{2/3}Fe_{1/3}Se_2$ shows improved redox properties intrinsically. All the electrochemical results indicate that *c*-$Co_{2/3}Fe_{1/3}Se_2$ could be a better choice as an OER catalyst. The OER performance of Co_2Fe_1-LDH is provided in **Figure S6**, of which overpotential is small bigger that of *c*-$Co_{2/3}Fe_{1/3}Se_2$.

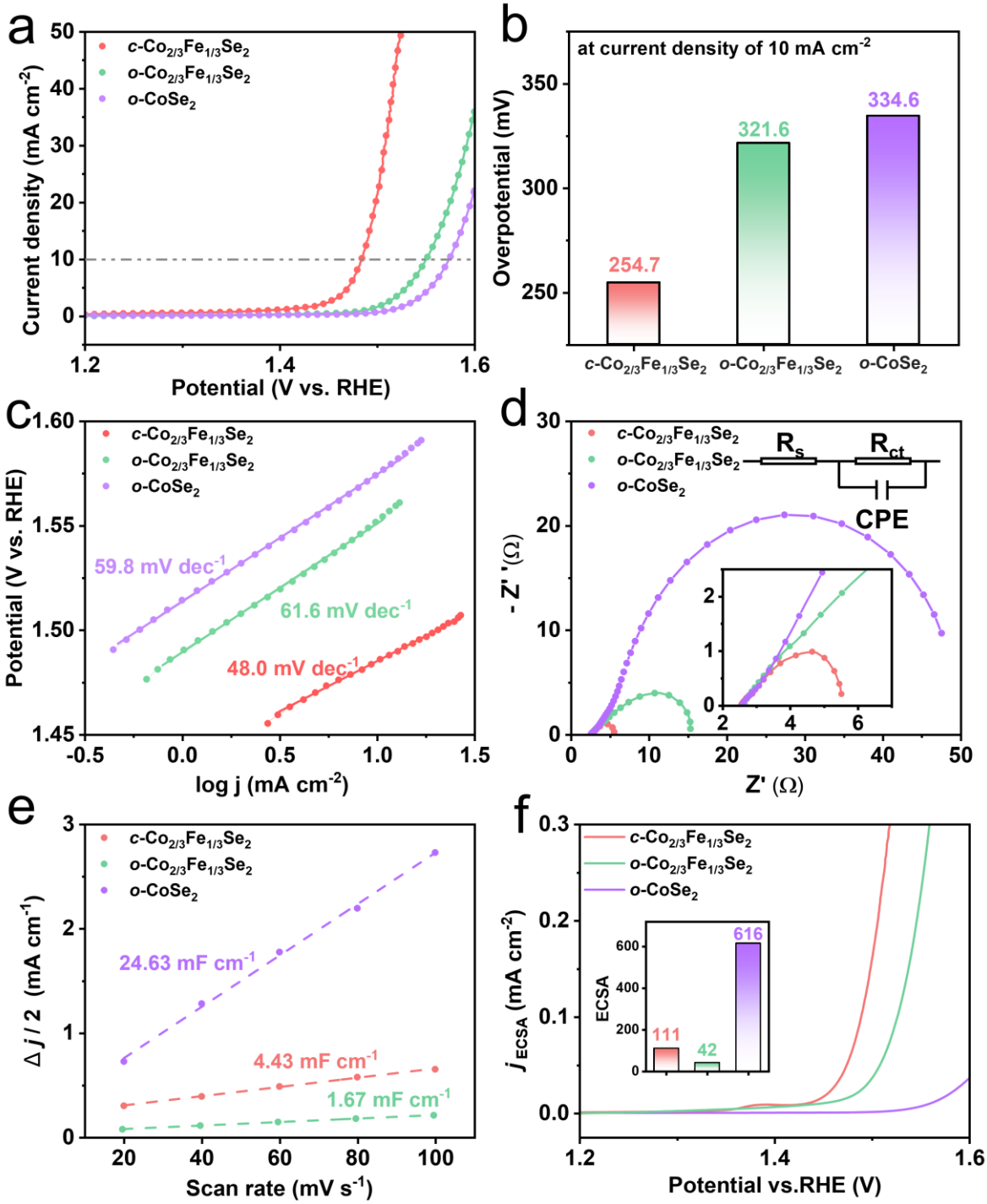

Figure 4. Electrochemical OER performance in 1.0 M KOH electrolyte. (a) LSV curves with iR-correction, (b) Overpotentials delivering 10 mA cm^{-2}, (c) Tafel slopes, (d) Nyquist plots, (e) C_{dl} values and (f) LSV curves normalized by ECSA, the insert in (f) shows the estimated ECSA values according to (e).

Earlier studies demonstrated that metal selenides will convert into the corresponding hydroxide and then serve as the actual active phase during OER process, however, further

relationships between surface structure and the electrocatalytic performance have been rarely studied in detail. [17, 18, 19, 33]. Herein, the surface-active phase transformation was investigated by *ex-situ* experiments. Chronopotentiometry (CP) test was first estimated at a fixed current density of 20 mA cm^{-2} at room temperature to investigate the durability (**Figure 5**a). *c*-$Co_{2/3}Fe_{1/3}Se_2$ exhibits the lowest steady voltage of 1.520 V compared with that of *o*-$Co_{2/3}Fe_{1/3}Se_2$ (1.543V) and o-$CoSe_2$ (1.583V). It should be noted that the activity of all catalysts after a long-term test, as shown in Figure 5b, reveals an improved trend and the *c*-$Co_{2/3}Fe_{1/3}Se_2$ still possesses the best OER catalytic activity. This phenomenon is mainly attributed to the active species forming on the surface of primitive selenide catalysts. The C_{dl}, ECSA, and EIS values after CP test are provided in **Figure S7**. *o*-$CoSe_2$ still exhibits the largest C_{dl} value of 45 mF cm^{-1} and *c*-$Co_{2/3}Fe_{1/3}Se_2$ remains the highest intrinsic electrocatalytic activity. The ECSA of all catalysts exhibited an obvious increase (139 for *c*-$Co_{2/3}Fe_{1/3}Se_2$, 57 for *o*-$Co_{2/3}Fe_{1/3}Se_2$, and 505 for *o*-$CoSe_2$), confirming that the surface evolution is beneficial to the OER process. The Nyquist plots of three catalysts suggest the active species forming on the surface enhance the charge-transfer kinetics, and this influence on *o*-$CoSe_2$ is greatest. *c*-$Co_{2/3}Fe_{1/3}Se_2$ still exhibits the smallest R_{ct} value.

To further verify the surface evolution, inductively coupled plasma (ICP) technology was used to detect the ion components of the electrolyte after the CP test, as presented in Figure 5c. Se atoms were dissolved out substantially from selenide catalysts, implying the surface phase change during the continuous catalysis (Figure 5c, the Fe atoms in 1.0 M KOH electrolyte may be ascribed to the trace Fe in solid KOH). It should be noted that the Fe atoms in *c*-$Co_{2/3}Fe_{1/3}Se_2$ exude more massively compared with that of *o*-$Co_{2/3}Fe_{1/3}Se_2$, while the Co atoms in the three catalysts exhibit different degrees of dissolving. Moreover, the elemental compositions of the catalysts after the catalytic reaction were determined by EDS (**Figure S8**). The atoms ratio of Co: Fe: Se: O in *o*-$Co_{2/3}Fe_{1/3}Se_2$ is 14.6: 10.6: 11.3: 63, which further confirms that the Se atoms

dissolve out from the primitive catalyst partially during the limited test time. In comparison, *c*-$Co_{2/3}Fe_{1/3}Se_2$ exhibits a molar ratio of 21.9: 13.6: 1.1: 63.4, which suggests that almost all the Se atoms separate out. These findings drive us to link Fe atoms diffusion with surface evolution, both of which determine the OER performance. For cubic $CoSe_2$, the Fe atoms located at the Co lattice position will migrate to the surface more easily in alkaline media compared to the orthorhombic system, and a Co-Fe synergetic active species which possesses better OER activity compared with a single Co-contained active intermediate layer is thus formed. XPS spectra after the CP test were used to verify the surface chemical environment preliminarily. The survey spectra in **Figure S9** indicate the co-presence of Co and Fe elements while the signal of Se almost disappeared. Co 2p XPS spectra, as displayed in Figure 5d, demonstrate the disappearance of Co-Se bond compared with those in Figure 3c. The binding energy of Co species in *c*-$Co_{2/3}Fe_{1/3}Se_2$ after the CP test exhibits a positive shift compared with those of *o*-$Co_{2/3}Fe_{1/3}Se_2$ and *o*-$CoSe_2$, agreeing with some previous literature which declares high-valance Co species contribute to better OER activity. Detailed information suggests the Co is in +2 and +3 valence state after the CP test[36]. Fe 2p XPS spectra of *c*-$Co_{2/3}Fe_{1/3}Se_2$ and *o*-$Co_{2/3}Fe_{1/3}Se_2$, as shown in Figure 5e, almost overlap and indicate the disappearance of Se-Fe bonds. Surface Fe species is also in mixed +2/+3 valence states. Se 3d XPS spectra exhibit a big difference compared with primitive catalysis in the strength of metal-Se bond (Figure 5f), indicating the leaching out of Se atoms for the lattice. All the results suggest that Se atoms exude and a phase transformation into hydroxide occurs during the OER process.

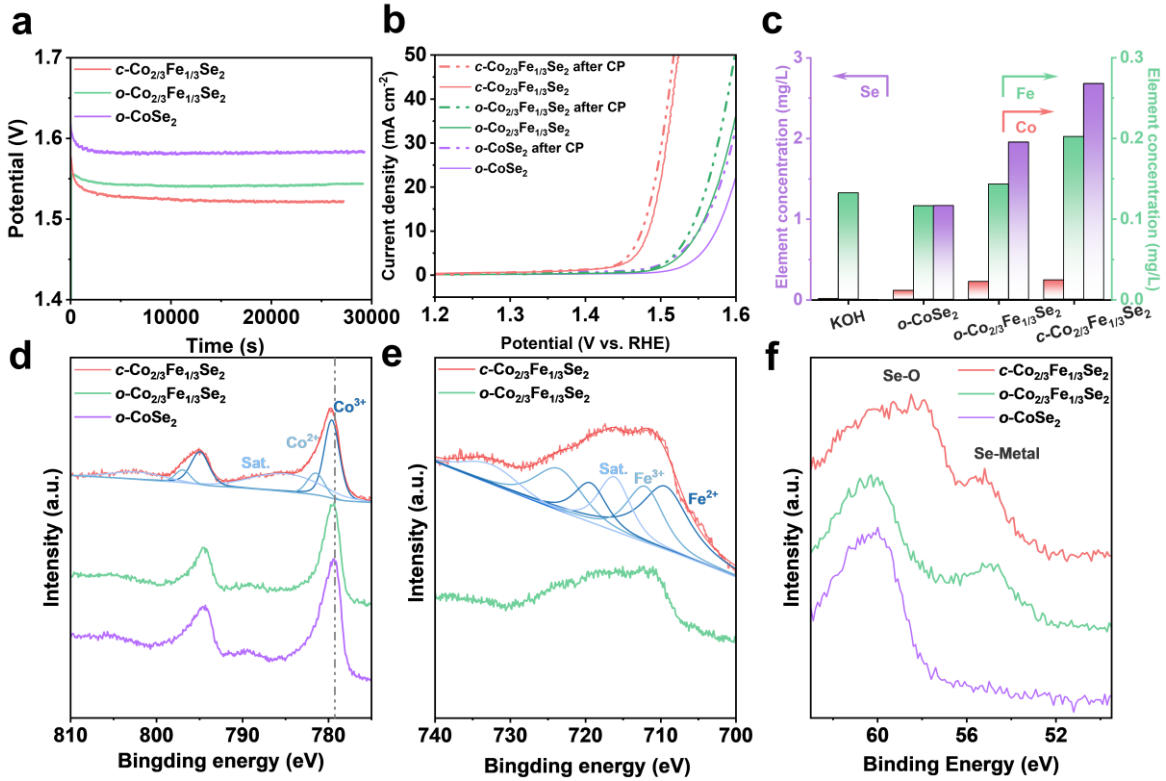

Figure 5. (a) Chronopotentiometry test at 20 mA cm^{-2}. (b) LSV curves before and after CP test. (c) Element concentration in electrolyte after CP test. (d) Co 3d, (e) Fe 2p, (f) Se 3d spectra after CP test.

Raman spectra were collected to further analyze the surface activity species. **Figure 6** provided the Raman before and after CP test. The spectra of *o*-$CoSe_2$ before and after CP test almost remained the same, indicating the bulk phase remains in the initial state during the OER process. On the contrary, the surface structure phases of *o*-$Co_{2/3}Fe_{1/3}Se_2$ and *c*-$Co_{2/3}Fe_{1/3}Se_2$ evolve dramatically and the characteristic Se-Se stretching bond at around 192 cm^{-1} even fades away for *c*-$Co_{2/3}Fe_{1/3}Se_2$, indicating the surface oxidation of different bulk structures is different from each other. This result matches well with the EDS data. Surface oxidation is vital to forming an active structure for non-oxide transition metal catalysts[37, 38]. Based on Raman and XPS results, it can be concluded that phase transformation indeed takes place for water oxidation. Since the effective measurement thickness of the Raman technology is about 10 nm, and the consisted components of the bulk catalyst (e.g. Fe and Co oxide, hydroxide phases, herein we will not further distinguish hydroxide and oxyhydroxide) are structurally similar, it

is rather difficult to identify the stretching bonds accurately. Even so, some early *in situ* studies are available to help us draw a general conclusion. The peak positions located at 266.4 cm^{-1}, 425 $cm^{-1,}$ and 504.5 cm^{-1} are attributed to Co $(OH)_2$ according to some existing work[39]. The bond at 457 nm^{-1} is ascribed to the M-OH translation mode which is similar to Co-Fe LDH[40]. The sharp peak observed at around 572.2 cm^{-1} is attributed to the formation of CoOOH which was regarded as an active intermediate phase for most Co-based OER catalysts[41, 42]. Alexis T. Bell demonstrated that the introduction of Fe atoms contributed to a blue shift at around 573 cm^{-1}, which might originate from Fe_3O_4, γ-Fe_2O_3, and γ-FeOOH, respectively[43, 44]. Based on the ICP data, EDS, and XPS results before and after CP test, it is speculated the Fe substitution will cause lattice distortion and accelerate the surface evolution during OER process. The lattice distortion of ⁻the cubic system is unstable in alkaline media and tends to form a hydroxide phase. For *c*-$Co_{2/3}Fe_{1/3}Se_2$ catalyst, the Fe atoms will migrate to the alkaline electrolyte more easily and participate in the Co oxidation on the surface, which contributes to much more active Co-Fe composite hydroxide. Numerous pieces of research have demonstrated that the introduction of Fe element will optimize the electronic structure of transition metal compound, which will further facilitate the oxygen intermediate adsorption/desorption processes and contribute to the improved OER activity[45, 46, 47].

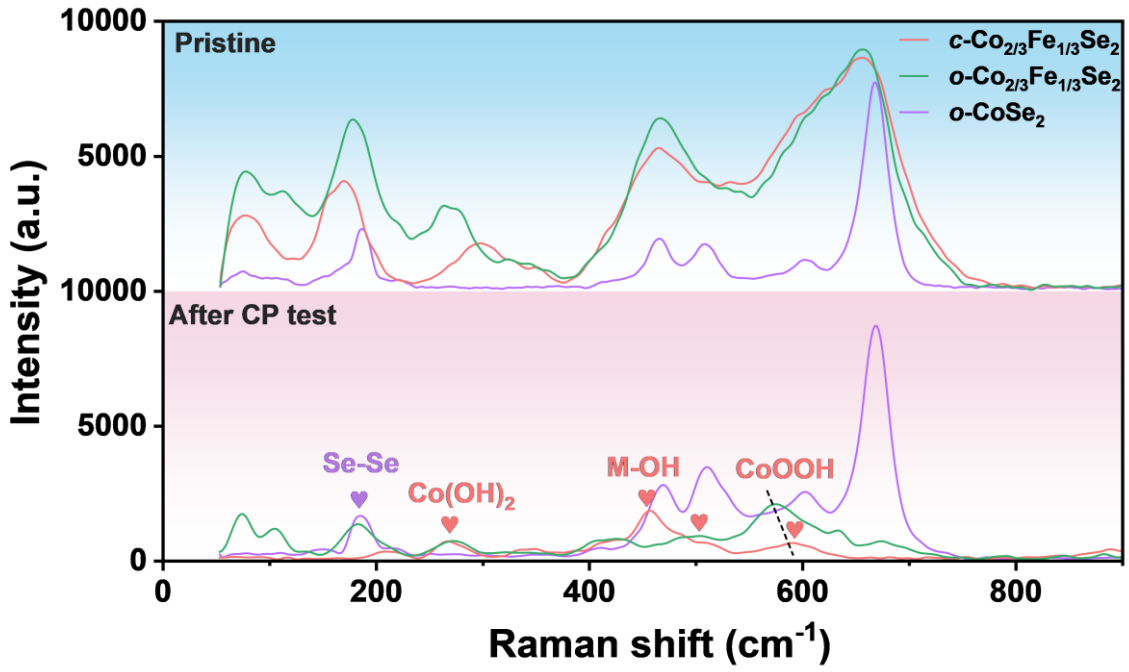

Figure 6. Raman spectra of catalysts before and after CP test

To obtain a deep insight into the OER catalytic mechanism on different selenide nanostructures, HRTEM images after a long-time CP test were also collected. As illustrated in **Figure 7**a-b, an amorphous oxidation layer was generated on the surface of *c*-$Co_{2/3}Fe_{1/3}Se_2$, and a core@shell-like structure was thus formed, identical well with XPS and Raman spectra results. Clear lattice planes with interspace values of 0.319 nm and 0.263 nm may correspond to the (120) plane of CoOOH (JCPDS #16-0480, space group *Pbnm*) and some planes of CoO_x (for instance, the (111) plane of cubic CoO JCPDS#42−1300, space group *F-43m*), separately. The associated fast Fourier transform (FFT) image with several diffraction rings suggests the partial layered and amorphous structure of the oxidation phase (insert in Figure 7a).

Local up-scaling HRTEM insert in Figure 7b reveals the packing method of ABCABC corresponding to the face-centered cubic phase structure, and the loss of Fe atoms contributes to several defects which may also affect the conductivity of core structure and further optimize catalytic activity[48, 49, 50]. Considering both the considerable conductivity of Co-based selenide with Se atom dissolution during the anodic OER process and the hydroxide shell layer

contacting with the electrolyte directly, it was thus reasonably speculated that the defects didn't influence OER activity to a great extent. The FFT image suggests the Se migration contributed to a certain degree of structural evolution compared with the diffraction pattern in Figure 2e. However, the core remains the cubic system. The HRTEM and corresponding FFT images of *o*-$CoSe_2$ and *o*-$Co_{2/3}Fe_{1/3}Se_2$ provided in Figure 7c-d suggest that only a thin oxidation layer existed and the orthorhombic bulk phases are well preserved, which could be further evidenced by the spot pattern in FFT images. This phenomenon demonstrates that *c*-$Co_{2/3}Fe_{1/3}Se_2$ turns to form a thicker oxidation layer (Co-Fe hydroxide) which is the real active species for OER process as illustrated in Figure 7e. It is common that the newly formed hydroxide layers are prone to amorphous when the non-hydroxide catalysts are under the anode current in alkaline media [17, 20, 51]. Compared with above ECSA results, it is suggested that there is an inverted relationship between ECSA and the surface oxidation evolution. It may be attributed to the exposed metal atoms, which play as the absorption sites in OER process[52, 53, 54]. For *o*-$Co_{2/3}Fe_{1/3}Se_2$, the surface evolution is poor and more Co and Fe atoms are exposed to the electrolyte. On the contrary, the surface of *c*-$Co_{2/3}Fe_{1/3}Se_2$ is more susceptible to evolution. However, the number of metal atoms in the layer hydroxide is much smaller than bulk phase.

In addition, to investigate the effect of Fe element content on OER activity, the molar ratio of Co/Fe raw material is further reduced to 4:1 and 8:1, separately. XRD patterns with different shifted deviations, as displayed in **Figure S10**, indicate Fe atoms cause small lattice contraction by replacing the Co atoms in the cubic lattice of $CoSe_2$. *c*-$Co_{2/3}Fe_{1/3}Se_2$ samples with a feed ratio of 4:1 and 8:1 need an overpotential of 284 and 317 mV to deliver the current density of 10 mA cm^{-2}, respectively, which are larger than 254.7 mV for *c*-$Co_{2/3}Fe_{1/3}Se_2$ with the ratio of 2:1, but superior to that of *o*-$Co_{2/3}Fe_{1/3}Se_2$ (321.6 mV) with the ratio of 2:1 (**Figure S11**). The Nyquist plots of *c*-$Co_{2/3}Fe_{1/3}Se_2$ with the ratio of 4:1 and 8:1 exhibit charge transfer resistance of 9.37 Ω and 21.70 Ω, separately, which suggests the introduction of Fe atoms in cubic $CoSe_2$

can also enhance electron transport capacity. This finding suggests the OER activity of $CoSe_2$ is strongly associated with the Fe content, and the *in situ* formed oxidation layer on the surface of *c*-$Co_{2/3}Fe_{1/3}Se_2$ is vital for efficient OER activity.

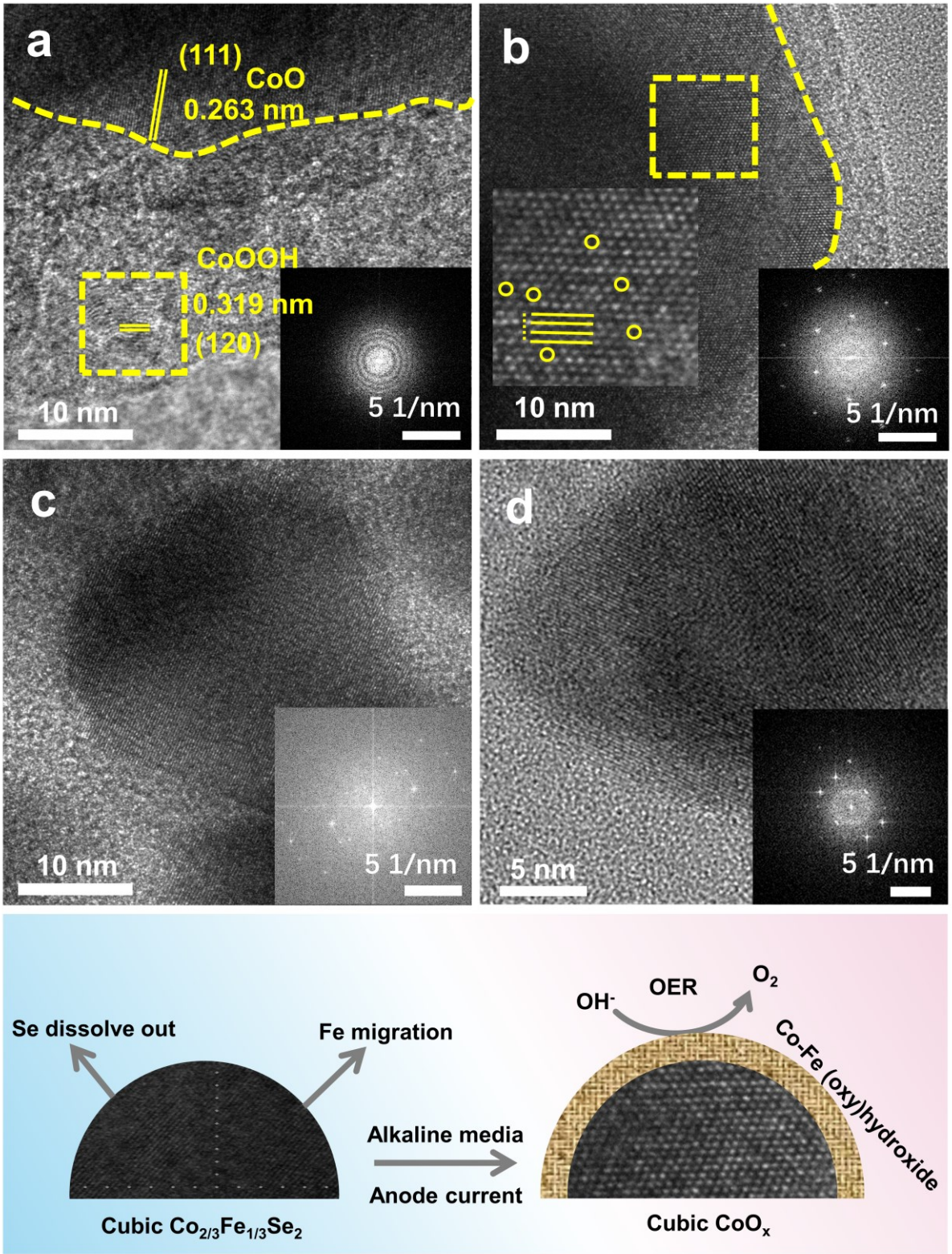

Figure 7. HRTEM images of (a-b) *c*-$Co_{2/3}Fe_{1/3}Se_2$, (c) *o*-$CoSe_2$ and (d) *o*-$Co_{2/3}Fe_{1/3}Se_2$ after the CP test, the inserts show the corresponding FFT patterns. (e) Schematic illustration of the catalyst surface oxidation mechanism for *c*-$Co_{2/3}Fe_{1/3}Se_2$ during the OER.

DFT calculations were used to reveal the role of the Fe atom regarding the electronic structure. Some previous works have claimed that there are hydroxide layers on the surface of selenides and oxides under the anode current[17, 19, 20, 55], which further confirms our opinion. The (001) surface $Co(OH)_2$ with a space group of *P-3m1* is selected as the model and the same surface exposed and replaced the Co atom to obtain CoFe hydroxide[56, 57]. The calculation results are elaborated in **Figure 8**. In consideration of the atom difference charge density in the slice of (001) (Figure 8a, 8b), Fe atoms possess lower electron density compared with Co. It is suggested that the Fe atoms will lose more electrons and are prone to exhibit a higher valence state during the surface evolution takes place. Furthermore, we visualized the Mulliken charge quantitative value (Figure 8c). There are two equivalent positions for Co atoms, the nearest position to Fe atoms was named Co1, and the remote position Co2. The value for Fe atoms is 1.08 which is bigger than that of Co1 (0.95) and Co2 (0.98). It can be concluded that the inducing of Fe will endow the nearest Co atoms with more electrons and this function will be weak when applied to remote atoms. Finally, the Density of states (DOS) and d band (Figure 8d, 8e, 8f) is calculated. Clearly, near the Fermi lever, the charge density mainly originates from the d band which confirms the d-band Theory[58, 59]. Maybe because of the near-atomic number and the small number of introduction Fe atoms, the total DOS could not exhibit very different, as well as the d-band centre. Specifically, the value of the d-band centre for CoFe hydroxide is -1.25 eV and -1.30 eV for Co hydroxide. Small rise indicates stronger absorption ability and it is beneficial for the stability of intermediates[60]. The d-band partial DOS (PDOS) for different atoms was also displayed (Figure 8f). There is an obvious conjugate action for Fe and Co atoms

and an energy shift, which indicates Fe improves the chemical environment of Co and it is consistent with Mulliken charge result.

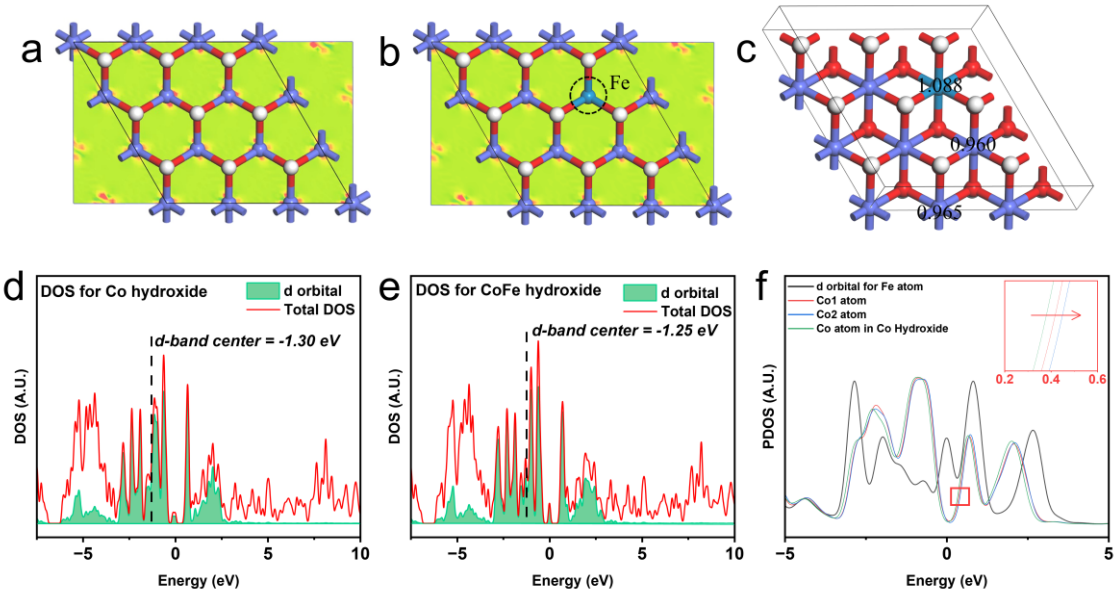

Figure 8. Theoretical calculations. Differential charge densities of (a) Co hydroxide and (b) CoFe hydroxide, in which the red contours represent electron accumulation. (c) The Mulliken charge of CoFe hydroxide. DOS of (d) Co hydroxide and (e) CoFe hydroxide. (f) Site-dependent PDOS of d orbitals in CoFe and Co hydroxide.

4. Conclusion

In summary, Fe dopant could induce the phase transition of $CoSe_2$ from orthorhombic to cubic symmetry during the selenylation process of the LDH precursor. *c*-$Co_{2/3}Fe_{1/3}Se_2$ exhibits an outstanding electrocatalytic activity in 1.0 M KOH with an overpotential of 254.7 mV delivering a current density of 10 mA cm^{-2} and a Tafel slope of 48.0 mV dec^{-1}, overpassing both *o*-$Co_{2/3}Fe_{1/3}Se_2$ and *o*-$CoSe_2$. The *ex-situ* characterizations before and after the OER process show that the Fe dopant in *c*-$Co_{2/3}Fe_{1/3}Se_2$ efficiently promotes the *in-situ* formation of thin Co-Fe hydroxide layers on the surface of the catalyst and thus endows the enhanced OER activity. DFT calculations reveal that Fe atoms in CoFe hydroxide are in high value and tune

the charge density of Co atoms and enhance the absorption capacity to intermediate. These findings unveil the relationship between the surface structure and the electrocatalytic performance during the anodic OER process, which may open a new door to designing advanced electrocatalysts based on transition metal elements.

Declaration of Competing Interest

The authors declare that they have no known competing financial interests or personal relationships that could have appeared to influence the work reported in this paper.

Data Availability

Data will be made available on request.

Acknowledgment

This work is financially supported by the National Natural Science Foundation of China (U20A20123 and 51874357) and Hunan Provincial Natural Science Foundation of China (2019JJ10006). H. W. thanks the support from the Project of Zhongyuan Critical Metals Laboratory (GJJSGFYQ202336) and the Youth Talent Program of Zhengzhou University (32340398).

Appendix A. Supporting information

Supplementary data associated with this article can be found in the online version at:

References

(1) Seh, Z. W.; Kibsgaard, J.; Dickens, C. F.; Chorkendorff, I.; Norskov, J. K.; Jaramillo, T. F. Combining theory and experiment in electrocatalysis: Insights into materials design. *Science* **2017**, *355* (6321), eaad4998.
(2) Jiao, K.; Xuan, J.; Du, Q.; Bao, Z.; Xie, B.; Wang, B.; Zhao, Y.; Fan, L.; Wang, H.; Hou, Z.; et al. Designing the next generation of proton-exchange membrane fuel cells. *Nature* **2021**, *595* (7867), 361-369.
(3) Lin, Z.; Wang, Z.; Gong, J.; Jin, T.; Shen, S.; Zhang, Q.; Wang, J.; Zhong, W. Reversed Spillover Effect Activated by Pt Atom Dimers Boosts Alkaline Hydrogen Evolution Reaction. *Adv. Funct. Mater.* **2023**, *33* (45).
(4) Suen, N. T.; Hung, S. F.; Quan, Q.; Zhang, N.; Xu, Y. J.; Chen, H. M. Electrocatalysis for the oxygen evolution reaction: recent development and future perspectives. *Chem. Soc. Rev.* **2017**, *46* (2), 337-365.
(5) He, Y.; Jia, L.; Lu, X.; Wang, C.; Liu, X.; Chen, G.; Wu, D.; Wen, Z.; Zhang, N.; Yamauchi, Y.; et al. Molecular-Scale Manipulation of Layer Sequence in Heteroassembled Nanosheet Films toward Oxygen Evolution Electrocatalysts. *ACS Nano* **2022**, *16* (3), 4028-4040.
(6) Zheng, Z.; Guo, Y.; Wan, H.; Chen, G.; Zhang, N.; Ma, W.; Liu, X.; Liang, S.; Ma, R. Anchoring Active Sites by Pt2FeNi Alloy Nanoparticles on NiFe Layered Double Hydroxides for Efficient Electrocatalytic Oxygen Evolution Reaction. *Energy Environ. Mater.* **2021**, *5* (1), 270-277.
(7) Sakai, N.; Fukuda, K.; Ma, R.; Sasaki, T. Synthesis and Substitution Chemistry of Redox-Active Manganese/Cobalt Oxide Nanosheets. *Chem. Mater.* **2018**, *30* (5), 1517-1523.
(8) Chen, G.; Wan, H.; Ma, W.; Zhang, N.; Cao, Y.; Liu, X.; Wang, J.; Ma, R. Layered Metal Hydroxides and Their Derivatives: Controllable Synthesis, Chemical Exfoliation, and Electrocatalytic Applications. *Adv. Energy Mater.* **2019**, *10* (11), 1902535.
(9) Chen, G.; Liaw, S. S.; Li, B.; Xu, Y.; Dunwell, M.; Deng, S.; Fan, H.; Luo, H. Microwave-assisted synthesis of hybrid CoxNi1−x(OH)2 nanosheets: Tuning the composition for high performance supercapacitor. *J. Power Sources* **2014**, *251* (1), 338-343.
(10) Chen, S.; Zheng, Z.; Li, Q.; Wan, H.; Chen, G.; Zhang, N.; Liu, X.; Ma, R. Boosting electrocatalytic water oxidation of NiFe layered double hydroxide via the synergy of 3d–4f electron interaction and citrate intercalation. *J. Mater. Chem. A* **2023**, *11* (4), 1944-1953.
(11) Hegazy, M. B. Z.; Berber, M. R.; Yamauchi, Y.; Pakdel, A.; Cao, R.; Apfel, U. P. Synergistic Electrocatalytic Hydrogen Evolution in Ni/NiS Nanoparticles Wrapped in Multi-Heteroatom-Doped Reduced Graphene Oxide Nanosheets. *ACS Appl. Mater. Interfaces* **2021**, *13* (29), 34043-34052.
(12) Shen, S.; Wang, Z.; Lin, Z.; Song, K.; Zhang, Q.; Meng, F.; Gu, L.; Zhong, W. Crystalline-Amorphous Interfaces Coupling of CoSe2 /CoP with Optimized d-band Center and Boosted Electrocatalytic Hydrogen Evolution. *Adv. Mater.* **2022**, *34* (13), e2110631.
(13) Chen, S.; Zheng, Z.; Wang, F.; Wan, H.; Chen, G.; Zhang, N.; Liu, X.; Ma, R. Tuning the Electronic Structure of Cobalt–Ruthenium Phosphide Nanosheets for Efficient Overall Water Splitting. *ACS Sustainable Chem. Eng.* **2022**, *10* (48), 15889-15897.
(14) Mabayoje, O.; Shoola, A.; Wygant, B. R.; Mullins, C. B. The Role of Anions in Metal Chalcogenide Oxygen Evolution Catalysis: Electrodeposited Thin Films of Nickel Sulfide as "Pre-catalysts". *ACS Energy Lett.* **2016**, *1* (1), 195-201.
(15) Chen, G.; Hu, Z.; Zhu, Y.; Gu, B.; Zhong, Y.; Lin, H. J.; Chen, C. T.; Zhou, W.; Shao, Z. A Universal Strategy to Design Superior Water-Splitting Electrocatalysts Based on Fast In Situ Reconstruction of Amorphous Nanofilm Precursors. *Adv. Mater.* **2018**, *30* (43), e1804333.
(16) Chen, W.; Liu, Y.; Li, Y.; Sun, J.; Qiu, Y.; Liu, C.; Zhou, G.; Cui, Y. In Situ Electrochemically Derived Nanoporous Oxides from Transition Metal Dichalcogenides for

Active Oxygen Evolution Catalysts. *Nano Lett.* **2016**, *16* (12), 7588-7596.
(17) Xu, K.; Ding, H.; Lv, H.; Tao, S.; Chen, P.; Wu, X.; Chu, W.; Wu, C.; Xie, Y. Understanding Structure-Dependent Catalytic Performance of Nickel Selenides for Electrochemical Water Oxidation. *ACS Catal.* **2016**, *7* (1), 310-315.
(18) Xu, X.; Song, F.; Hu, X. A nickel iron diselenide-derived efficient oxygen-evolution catalyst. *Nat. Commun.* **2016**, *7* (1), 12324.
(19) Zhu, Y.; Chen, H.-C.; Hsu, C.-S.; Lin, T.-S.; Chang, C.-J.; Chang, S.-C.; Tsai, L.-D.; Chen, H. M. Operando Unraveling of the Structural and Chemical Stability of P-Substituted CoSe2 Electrocatalysts toward Hydrogen and Oxygen Evolution Reactions in Alkaline Electrolyte. *ACS Energy Lett.* **2019**, *4* (4), 987-994.
(20) Fabbri, E.; Nachtegaal, M.; Binninger, T.; Cheng, X.; Kim, B. J.; Durst, J.; Bozza, F.; Graule, T.; Schaublin, R.; Wiles, L.; et al. Dynamic surface self-reconstruction is the key of highly active perovskite nano-electrocatalysts for water splitting. *Nat. Mater.* **2017**, *16* (9), 925-931.
(21) Sun, Y.; Li, X.; Zhang, T.; Xu, K.; Yang, Y.; Chen, G.; Li, C.; Xie, Y. Nitrogen-Doped Cobalt Diselenide with Cubic Phase Maintained for Enhanced Alkaline Hydrogen Evolution. *Angew. Chem. Int. Ed.* **2021**, *60* (39), 21575-21582.
(22) Chen, P.; Xu, K.; Tao, S.; Zhou, T.; Tong, Y.; Ding, H.; Zhang, L.; Chu, W.; Wu, C.; Xie, Y. Phase-Transformation Engineering in Cobalt Diselenide Realizing Enhanced Catalytic Activity for Hydrogen Evolution in an Alkaline Medium. *Adv. Mater.* **2016**, *28* (34), 7527-7532.
(23) Zheng, Y. R.; Wu, P.; Gao, M. R.; Zhang, X. L.; Gao, F. Y.; Ju, H. X.; Wu, R.; Gao, Q.; You, R.; Huang, W. X.; et al. Doping-induced structural phase transition in cobalt diselenide enables enhanced hydrogen evolution catalysis. *Nat. Commun.* **2018**, *9* (1), 2533.
(24) Ma, W.; Ma, R.; Wang, C.; Liang, J.; Liu, X.; Zhou, K.; Sasaki, T. A Superlattice of Alternately Stacked Ni–Fe Hydroxide Nanosheets and Graphene for Efficient Splitting of Water. *ACS Nano* **2015**, *9* (2), 1977-1984.
(25) Kang, H.; Li, H.; Zhao, X.; Yang, L.; Xu, S. Anion doped bimetallic selenide as efficient electrocatalysts for oxygen evolution reaction. *Ceram. Int.* **2020**, *46* (3), 2792-2797.
(26) Yuan, B.; Luan, W.; Tu, S. T. One-step synthesis of cubic FeS2 and flower-like FeSe2 particles by a solvothermal reduction process. *Dalton Trans.* **2012**, *41* (3), 772-776.
(27) Opacic, M.; Lazarevic, N. Lattice dynamics of iron chalcogenides: Raman scattering study. *J. Serb. Chem. Soc.* **2017**, *82* (9), 957-983.
(28) Shan, H.; Qin, J.; Ding, Y.; Sari, H. M. K.; Song, X.; Liu, W.; Hao, Y.; Wang, J.; Xie, C.; Zhang, J.; et al. Controllable Heterojunctions with a Semicoherent Phase Boundary Boosting the Potassium Storage of CoSe2 /FeSe2. *Adv. Mater.* **2021**, *33* (37), e2102471.
(29) Kong, D.; Wang, H.; Lu, Z.; Cui, Y. CoSe2 nanoparticles grown on carbon fiber paper: an efficient and stable electrocatalyst for hydrogen evolution reaction. *J. Am. Chem. Soc.* **2014**, *136* (13), 4897-4900.
(30) Shen, S.; Zhang, H.; Song, K.; Wang, Z.; Shang, T.; Gao, A.; Zhang, Q.; Gu, L.; Zhong, W. Multi-d Electron Synergy in LaNi(1-x) Co(x) Ru Intermetallics Boosts Electrocatalytic Hydrogen Evolution. *Angew. Chem. Int. Ed. Engl.* **2024**, *63* (1), e202315340.
(31) Yao, N.; Wang, G.; Jia, H.; Yin, J.; Cong, H.; Chen, S.; Luo, W. Intermolecular Energy Gap-Induced Formation of High-Valent Cobalt Species in CoOOH Surface Layer on Cobalt Sulfides for Efficient Water Oxidation. *Angew. Chem. Int. Ed.* **2022**, *61* (28), e202117178.
(32) Kwak, I. H.; Im, H. S.; Jang, D. M.; Kim, Y. W.; Park, K.; Lim, Y. R.; Cha, E. H.; Park, J. CoSe(2) and NiSe(2) Nanocrystals as Superior Bifunctional Catalysts for Electrochemical and Photoelectrochemical Water Splitting. *ACS Appl. Mater. Interfaces* **2016**, *8* (8), 5327-5334.
(33) Sun, Y.; Xu, K.; Wei, Z.; Li, H.; Zhang, T.; Li, X.; Cai, W.; Ma, J.; Fan, H. J.; Li, Y. Strong Electronic Interaction in Dual-Cation-Incorporated NiSe2 Nanosheets with Lattice Distortion for Highly Efficient Overall Water Splitting. *Adv. Mater.* **2018**, *30* (35), e1802121.
(34) Bandal, H. A.; Jadhav, A. R.; Tamboli, A. H.; Kim, H. Bimetallic iron cobalt oxide self-

supported on Ni-Foam: An efficient bifunctional electrocatalyst for oxygen and hydrogen evolution reaction. *Electrochim. Acta* **2017**, *249* (20), 253-262.
(35) McCrory, C. C.; Jung, S.; Peters, J. C.; Jaramillo, T. F. Benchmarking heterogeneous electrocatalysts for the oxygen evolution reaction. *J. Am. Chem. Soc.* **2013**, *135* (45), 16977-16987.
(36) Wang, C.; Qi, L. Heterostructured Inter-Doped Ruthenium-Cobalt Oxide Hollow Nanosheet Arrays for Highly Efficient Overall Water Splitting. *Angew. Chem. Int. Ed.* **2020**, *59* (39), 17219-17224.
(37) Zhang, Y.; Ouyang, B.; Xu, J.; Jia, G.; Chen, S.; Rawat, R. S.; Fan, H. J. Rapid Synthesis of Cobalt Nitride Nanowires: Highly Efficient and Low-Cost Catalysts for Oxygen Evolution. *Angew. Chem. Int. Ed.* **2016**, *55* (30), 8670-8674.
(38) Xu, K.; Chen, P.; Li, X.; Tong, Y.; Ding, H.; Wu, X.; Chu, W.; Peng, Z.; Wu, C.; Xie, Y. Metallic nickel nitride nanosheets realizing enhanced electrochemical water oxidation. *J. Am. Chem. Soc.* **2015**, *137* (12), 4119-4125.
(39) Sun, F.; Li, C.; Li, B.; Lin, Y. Amorphous MoSx developed on Co(OH)2 nanosheets generating efficient oxygen evolution catalysts. *J. Mater. Chem. A* **2017**, *5* (44), 23103-23114.
(40) Liu, S.; Zhu, J.; Sun, M.; Ma, Z.; Hu, K.; Nakajima, T.; Liu, X.; Schmuki, P.; Wang, L. Promoting the hydrogen evolution reaction through oxygen vacancies and phase transformation engineering on layered double hydroxide nanosheets. *J. Mater. Chem. A* **2020**, *8* (5), 2490-2497.
(41) Jing Yang; Hongwei Liu; Wayde N. Martens; Frost, R. L. Synthesis and Characterization of Cobalt Hydroxide, Cobalt Oxyhydroxide, and Cobalt Oxide Nanodiscs. *J. Phys. Chem. C.* **2010**, *114* (1), 111-119.
(42) Tung, C. W.; Hsu, Y. Y.; Shen, Y. P.; Zheng, Y.; Chan, T. S.; Sheu, H. S.; Cheng, Y. C.; Chen, H. M. Reversible adapting layer produces robust single-crystal electrocatalyst for oxygen evolution. *Nat. Commun.* **2015**, *6* (1), 8106.
(43) Louie, M. W.; Bell, A. T. An investigation of thin-film Ni-Fe oxide catalysts for the electrochemical evolution of oxygen. *J. Am. Chem. Soc.* **2013**, *135* (33), 12329-12337.
(44) D. Thierry; D. Persson; C. Leygraf; N. Boucherit; A. Hugot-le Goff. Raman spectroscopy and XPS investigations of anodic corrosion films formed on FeMo alloys in alkaline solutions,. *Corros. Sci.* **1991**, *32* (3), 273-284.
(45) Trotochaud, L.; Young, S. L.; Ranney, J. K.; Boettcher, S. W. Nickel-iron oxyhydroxide oxygen-evolution electrocatalysts: the role of intentional and incidental iron incorporation. *J. Am. Chem. Soc.* **2014**, *136* (18), 6744-6753.
(46) Gorlin, M.; Ferreira de Araujo, J.; Schmies, H.; Bernsmeier, D.; Dresp, S.; Gliech, M.; Jusys, Z.; Chernev, P.; Kraehnert, R.; Dau, H.; et al. Tracking Catalyst Redox States and Reaction Dynamics in Ni-Fe Oxyhydroxide Oxygen Evolution Reaction Electrocatalysts: The Role of Catalyst Support and Electrolyte pH. *J. Am. Chem. Soc.* **2017**, *139* (5), 2070-2082.
(47) Xiao, H.; Shin, H.; Goddard, W. A., 3rd. Synergy between Fe and Ni in the optimal performance of (Ni,Fe)OOH catalysts for the oxygen evolution reaction. *Proc. Natl. Acad. Sci. U.S.A.* **2018**, *115* (23), 5872-5877.
(48) Dou, Y.; He, C. T.; Zhang, L.; Yin, H.; Al-Mamun, M.; Ma, J.; Zhao, H. Approaching the activity limit of CoSe2 for oxygen evolution via Fe doping and Co vacancy. *Nat Commun* **2020**, *11* (1), 1664.
(49) Wang, M.; Zhang, W.; Zhang, F.; Zhang, Z.; Tang, B.; Li, J.; Wang, X. Theoretical Expectation and Experimental Implementation of In Situ Al-Doped CoS2 Nanowires on Dealloying-Derived Nanoporous Intermetallic Substrate as an Efficient Electrocatalyst for Boosting Hydrogen Production. *ACS Catal.* **2019**, *9* (2), 1489-1502.
(50) Zhou, Z.; Xu, T.; Zhang, C.; Li, S.; Xu, J.; Sun, L.; Gao, L. Enhancing stability by tuning element ratio in 2D transition metal chalcogenides. *Nano Research* **2020**, *14* (6), 1704-1710.
(51) D'Olimpio, G.; Nappini, S.; Vorokhta, M.; Lozzi, L.; Genuzio, F.; Menteş, T. O.; Paolucci, V.; Gürbulak, B.; Duman, S.; Ottaviano, L.; et al. Enhanced Electrocatalytic Activity in GaSe

and InSe Nanosheets: The Role of Surface Oxides. *Adv. Funct. Mater.* **2020**, *30* (43).
(52) Yu, J.; He, Q.; Yang, G.; Zhou, W.; Shao, Z.; Ni, M. Recent Advances and Prospective in Ruthenium-Based Materials for Electrochemical Water Splitting. *ACS Catal.* **2019**, *9* (11), 9973-10011.
(53) You, B.; Liu, X.; Jiang, N.; Sun, Y. A General Strategy for Decoupled Hydrogen Production from Water Splitting by Integrating Oxidative Biomass Valorization. *J. Am. Chem. Soc.* **2016**, *138* (41), 13639-13646.
(54) Smith, R. D.; Berlinguette, C. P. Accounting for the Dynamic Oxidative Behavior of Nickel Anodes. *J. Am. Chem. Soc.* **2016**, *138* (5), 1561-1567.
(55) Sun, Y.; Mao, K.; Shen, Q.; Zhao, L.; Shi, C.; Li, X.; Gao, Y.; Li, C.; Xu, K.; Xie, Y. Surface Electronic Structure Modulation of Cobalt Nitride Nanowire Arrays via Selenium Deposition for Efficient Hydrogen Evolution. *Adv. Funct. Mater.* **2021**.
(56) Chen, P.; Zhou, T.; Wang, S.; Zhang, N.; Tong, Y.; Ju, H.; Chu, W.; Wu, C.; Xie, Y. Dynamic Migration of Surface Fluorine Anions on Cobalt-Based Materials to Achieve Enhanced Oxygen Evolution Catalysis. *Angew. Chem. Int. Ed. Engl.* **2018**, *57* (47), 15471-15475.
(57) Burke, M. S.; Kast, M. G.; Trotochaud, L.; Smith, A. M.; Boettcher, S. W. Cobalt-iron (oxy)hydroxide oxygen evolution electrocatalysts: the role of structure and composition on activity, stability, and mechanism. *J. Am. Chem. Soc.* **2015**, *137* (10), 3638-3648.
(58) Sun, S.; Zhou, X.; Cong, B.; Hong, W.; Chen, G. Tailoring the d-Band Centers Endows (NixFe1–x)2P Nanosheets with Efficient Oxygen Evolution Catalysis. *ACS Catal.* **2020**, *10* (16), 9086-9097.
(59) Chen, S.; Huang, H.; Jiang, P.; Yang, K.; Diao, J.; Gong, S.; Liu, S.; Huang, M.; Wang, H.; Chen, Q. Mn-Doped RuO2 Nanocrystals as Highly Active Electrocatalysts for Enhanced Oxygen Evolution in Acidic Media. *ACS Catal.* **2019**, *10* (2), 1152-1160.
(60) Wang, Z.; Lin, Z.; Wang, Y.; Shen, S.; Zhang, Q.; Wang, J.; Zhong, W. Nontrivial Topological Surface States in Ru(3) Sn(7) toward Wide pH-Range Hydrogen Evolution Reaction. *Adv. Mater.* **2023**, *35* (25), e2302007.

Graphical abstract

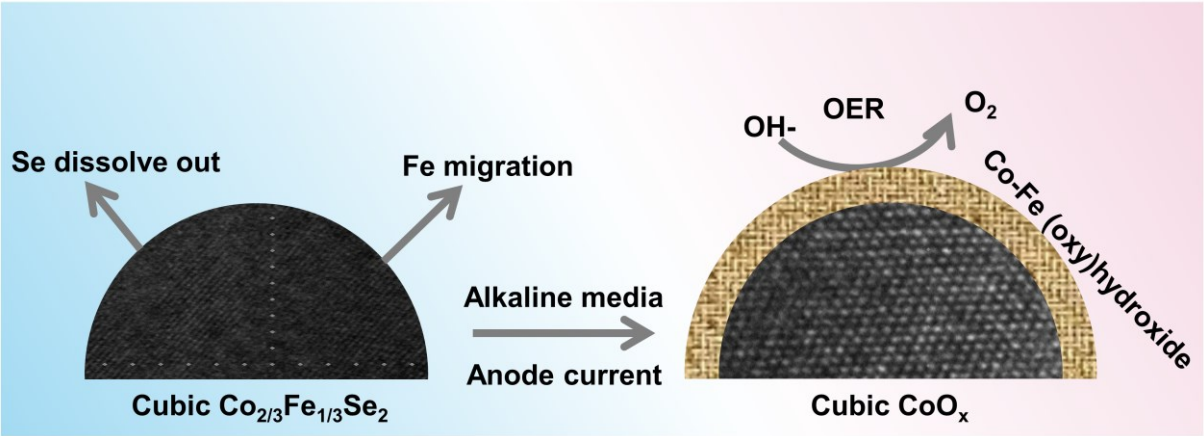

Our research puts forward new opinion for the surface evolution which is meaningful for high-performance catalysts design.